Journal of ELECTRONIC MATERIALS, Vol. 47, No. 2, 2018
https://doi.org/10.1007/s11664-017-5969-8

Simulation of SPS Process for Fabrication of Thermoelectric Materials with Predicted Properties

L.P. BULAT,[1] A.V. NOVOTELNOVA,[1] A.S. TUKMAKOVA,[1,5,6] D.E. YEREZHEP,[1] V.B. OSVENSKII,[2] A.I. SOROKIN,[2] V.P. PANCHENKO,[2] L.V. BOCHKOV,[3] and S. AŠMONTAS[4]

1.—Saint-Petersburg National Research University of Informational Technology, Mechanics and Optics (ITMO University), Lomonosova st. 9, aud. 3102, St. Petersburg, Russia 197101. 2.—GIREDMET Ltd, Tomilino, Moscow, Russia 119017. 3.—Ioffe Physical Technical Institute, St. Petersburg, Russia 194021. 4.—State Research Institute Center for Physical Science and Technology, 10222 Vilnius, Lithuania. 5.—e-mail: astukmakova@corp.ifmo.ru. 6.—e-mail: tukmashh@gmail.com

Spark plasma sintering (SPS) is a promising method for fabrication of thermoelectric materials. The electric and thermal fields in the SPS process have been simulated by using the finite element method to model an SPS-511S experimental setup. Investigation of thermoelectric materials based on Bi_2Te_3 solid solutions revealed that the temperature measured close to the sample during application of the electric current could be reproduced by the simulation. Modification of the compression mold configuration could be used to alter the electric and thermal conditions, adjust the Joule heat released in the setup elements, and create a gradient temperature field during the SPS process. The temperature–time dependence in the sample was also studied, revealing that the temperature difference along the vertical axis may reach hundreds of degrees. Prediction of the sintering temperature in each layer may allow further prediction of the thermoelectric properties of the sample. More accurate modifications of the SPS process based on such computer simulations may help to form structures with macroscopically inhomogeneous and functionally graded legs.

Key words: SPS, thermoelectrics, segmented materials, graded temperature field, finite element simulation

INTRODUCTION

Spark plasma sintering (SPS) is widely used for fabrication of various functional materials of micro- and nanopowders.[1] This method has been shown to be very convenient and effective for fabrication of nanostructures and nanocomposites.[1] SPS is also a perspective method for fabrication of bulk thermoelectric (TE) materials from ball-milled nanopowders.[2–4] In comparison with the hot-pressing method, the main advantage of SPS is the prevention of recrystallization that occurs during bulk sintering of nanothermoelectrics. Recrystallization can lead to an increase of the nanograin size from tens to hundreds of nanometers in bulk samples, changing the structure from nano- to microscale. This inhibits mechanisms that lead to improved thermoelectric properties of nanostructures, mainly decreased intensity of the additional phonon scattering observed on grain interfaces.[3,4] Accordingly, the phonon thermal conductivity increases while the thermoelectric figure of merit $ZT = \frac{\sigma\alpha^2}{\kappa}T$ decreases, where Z is the figure of merit, T is absolute temperature, and σ, κ, and α are the electrical conductivity, thermal conductivity, and Seebeck coefficient of the material used, respectively.

Use of segmented or functionally graded inhomogeneous materials can also increase the figure of merit. The operational vertical temperature

(Received December 15, 2016; accepted November 19, 2017; published online December 1, 2017)

difference $\Delta T_{z\ op.}$ in branches of thermoelectric generators can reach hundreds of degrees, with each thermoelectric material exhibiting its maximum figure of merit at a specific temperature. Therefore, it is expedient to make functionally graded or segmented legs in order to improve the performance of thermoelectric batteries.[5–7]

In Ref. 8, the output power of a segmented n-type sample fabricated from Bi_2Te_3 and $PbSe_{0.5}Te_{0.5}$ was about 15% and 73% higher than that of homogeneous Bi_2Te_3 and $PbSe_{0.5}Te_{0.5}$ samples, respectively, while $\Delta T_{z\ op.}$ varied from 300 K to 700 K. The output power increased with higher $\Delta T_{z\ op.}$. High-efficiency TE modules based on different segmented materials were investigated in Refs. 9 and 10, while an attempt to fabricate a TE generator using segmented two-layered legs was made in Ref. 11. Those legs, consisting of n-type Bi_2Te_3/$PbSe_{0.5}Te_{0.5}$ and p-type $Bi_{0.3}Sb_{1.7}Te_3/Zn_4Sb_3$, were fabricated without welding within one technological cycle of the SPS process in order to prevent material degradation.

To obtain segmented material, vertical variation of the sintering temperature within the sample $\Delta T_{z\ sint}$ should exist during the SPS process. Computer simulations can provide deeper comprehension of the dynamics of such temperature fields. Moreover, direct temperature measurements within the sample cannot be achieved using traditional experimental methods.

Finite element modeling of sintering of bismuth telluride could reproduce experimental sintering temperature values.[12–15] In particular, good agreement was achieved between the calculated sintering temperature for homogeneous Bi_2Te_3-Sb_2Te_3 samples and the experimental value of T_{sint} = 770 K; ZT = 1.23 to 1.25 at T_{sint} = 360 K was achieved experimentally for nanostructured samples based on $Bi_{0.4}Sb_{1.6}Te_3$ fabricated by ball milling followed by SPS under pressure of 50 MPa.[12] Inclusions with different electric and thermal conductivities, localized and distributed in the material volume, did not essentially influence the temperature fields in the sintered sample at macrolevel, although they changed the profile of the electric current density distribution.[14] Thus, compositional inhomogeneity did not influence the temperature field formation. Homogeneous material can be used during simulations of the temperature field distribution in inhomogeneous samples, and there is the basic possibility to create a vertical temperature gradient in a sample by changing the sample or die geometry.[12,15]

Few papers exist on the theory and simulation of sintering of nanothermoelectrics. Therefore, study of the temperature fields during the SPS remains an unaddressed problem. In the present study, we used the finite element method to simulate SPS of segmented thermoelectric nanomaterials in a gradient temperature field during one technological cycle.

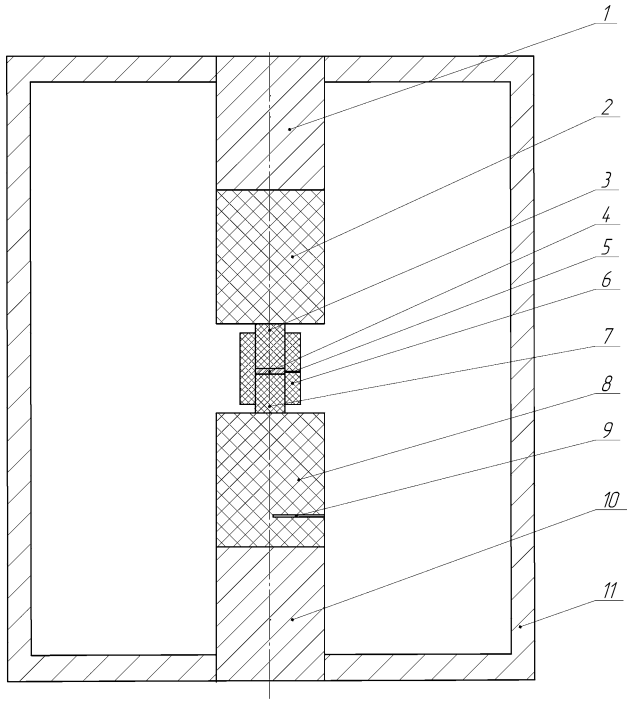

Fig. 1. Schematic model of SPS setup. 1, top cooled electrode (d_e = 80 mm, h_e = 60 mm); 2, top graphite insert (d_g = 80 mm, h_g = 60 mm); 3, top graphite punch (d_p = 20 mm; h_p = 20 mm); 4, sample (h_s = 10 mm, d_s = 20 mm); 5, aperture for thermocouple TC1; 6, cylindrical compression mold (wall thickness d_w = 20 mm, h_m = 40 mm); 7, bottom graphite punch (d_p = 20 mm, h_p = 20 mm); 8, bottom graphite insert (d_g = 80 mm, h_g = 60 mm); 9, aperture for thermocouple TC2; 10, bottom cooled electrode (d_e = 80 mm, h_e = 60 mm); 11, vacuum chamber.

SIMULATION MODEL

Calculations were carried out using COMSOL Multiphysics software for the SPS-511S experimental setup[3,4] using a two-dimensional (2D) axisymmetric geometry. The mesh consisted of 3520 domain elements of triangular shape and 331 boundary elements. The default, physics-controlled mesh sequence was used.

The modeled installation consists of a vacuum chamber with steel electrodes cooled by water (Fig. 1). The compression mold (6), which is fixed by graphite inserts (2 and 8), is placed between steel electrodes (1 and 10). The sintered sample (4) is set between graphite punches (3 and 7). Reliable contact is maintained by graphite foil linings, placed between the steel electrodes and graphite inserts, and a graphite foil tube, placed inside the compression mold.

The simulation was time dependent and included the system of differential equations describing the distribution of electric potential and temperature. The electric current density $\mathbf{j}$ and heat flow density $\mathbf{q}$ are related to their gradients according to the generalized laws of thermal and electrical conductivity as follows[16]:

$$\boldsymbol{j} = -\sigma(\nabla\mu + S\nabla T), \qquad (1)$$

Table I. Materials properties used in the simulation

	κ (W/m-K)			σ (10^6 S/m)			C_p (J/kg-K)		
T (K)	Bi_2Te_3	Graphite	Steel	Bi_2Te_3	Graphite	Steel	Bi_2Te_3	Graphite	Steel
300	1.938	91.3	14.3	0.0816	0.068871	1.233	0.1555	800	485
400	1.604	90.2	16.2	0.0597	0.077942	1.1236	0.1626	995	500
500	2.03	84.6	17.9	0.0483	0.085179	1.0493	0.1695	1208	550
600	4.091	78	19.3	0.05138	0.090662	0.994	0.1764	1381	555
700	6.881	71.7	20.6	0.06351	0.094518	0.9515	0.1833	1518	560
800	9.738	65.9	21.9	0.08552	0.097087	0.9166	0.1902	1629	570
900	12.75	60.9	23	0.1098	0.098522	0.8881	0.1972	1718	595

S (10^6 V/K)		
Bi_2Te_3	Graphite	Steel
220	2.15	− 1.4
235	1.8	− 1.9
200	0.9	− 2.6
160	− 0.35	3.13
0.1833	− 1.7	− 3.42
0.1902	− 2.85	− 3.5
0.1972	− 3.5	− 3.6

$$\boldsymbol{q} = -\nabla \times (\kappa T + ST\boldsymbol{j}), \tag{2}$$

where $\nabla\mu$ is the gradient of the electrochemical potential and S is the Seebeck coefficient.

The law of conservation of charge takes the following form:

$$\mathrm{div}\,\boldsymbol{j} = 0. \tag{3}$$

Energy balance takes the form[17]

$$c_p\rho\frac{\partial T}{\partial t} + \mathrm{div} \times \boldsymbol{q} + \boldsymbol{j}\nabla\mu = 0, \tag{4}$$

where c_p and ρ are the specific thermal capacity and material density, respectively, t is time, and $\mathbf{j}\nabla\mu$ is the Joule heating.

In the experiment,[3,4] a pulsed direct current of up to 1000 A was used. The duration of an impulse was 3.3 ms, and the on/off time ratio was 2.2. Two periods of the current switching-off followed the package which consisted of 12 impulses. In the simulation model, the time dependence of the effective current density was applied as the boundary condition on the upper electrode end, while the electric potential on the bottom electrode had zero value. All lateral surfaces of the setup elements, including electrodes, punches, and the die, were electrically isolated.

Thermal boundary conditions corresponding to radiative heat removal from the lateral sides of the compression mold, graphite inserts, and electrodes were applied, as follows:

$$\boldsymbol{n}(q) = \varepsilon\sigma_{SB}\left(T_{amb}^4 - T_0^4\right), \tag{5}$$

where $\mathbf{n}$ is the normal vector, and $\sigma_{SB} = 5.670 \times 10^{-8}$ W m^{-2} K^{-4} is the Stefan–Boltzmann constant; the factors ε were taken from Ref. [13] as 0.75 and 0.675 for graphite and steel, respectively; the ambient temperature was $T_{amb} = 300$ K, and T_0 is the temperature of the external surfaces of the elements.

The following boundary condition was used for the convective heat exchange due to water cooling:

$$\boldsymbol{n}(\boldsymbol{q}) = h \times (T_{ext} - T_e), \tag{6}$$

where h is the heat transfer coefficient (370 W m^{-2} K), T_{ext} is the water temperature, and T_e is the electrode surface temperature.

The sample was made from homogeneous Bi_2Te_3.[14] The temperature dependence of the kinetic coefficients of the sample and setup materials was taken into account, because SPS runs over a wide temperature range; these dependences were taken from Refs. 12, 18, and 19 and are presented in Table I.

GRADED TEMPERATURE FIELD CREATION IN SPS PROCESS

We compared the data obtained from the simulation with experimental data, considering the temperature change with time as a key parameter.

The temperature distribution during the experiment was controlled by means of thermocouples TC1 and TC2 in the lower graphite insert and in the graphite die in channels 5 and 9, respectively (Fig. 1). The measurement points in the model were located at exactly the same places. Figure 2 shows

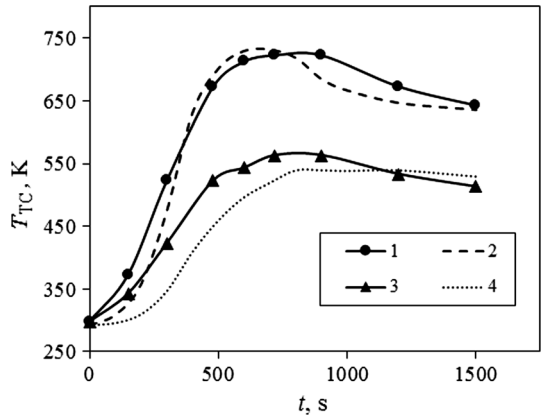

Fig. 2. Comparison of dependence of experimental and simulated temperature on time: 1, measured by TC1; 2, calculated; 3, measured by TC2; 4, calculated.

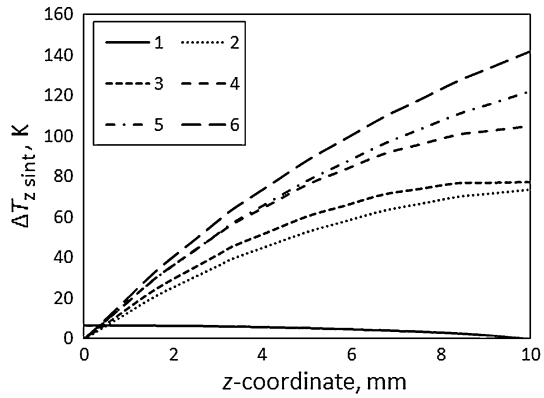

Fig. 3. Temperature distribution at t = 450 s along vertical axis in sample sintered in die with: 1, cylindrical profile (without any extension) and located as shown in Fig. 1; 2, cylindrical profile and in contact with the lower graphite insert; 3, concave profile; 4, conic profile; 5, curved profile; 6, step profile.

that sufficient agreement was obtained between the calculated and experimental results, which remained very similar throughout the sintering process. This verifies that the mathematical and physical descriptions of the model were correct. Based on this, further modification of the mold geometry in the simulation model could be conducted to reveal the gradient temperature field in the sample.

We investigated the impact of the compression mold location on the formation of the temperature field in the sample. If the mold was located as shown in Fig. 1, the temperature distribution was almost homogeneous, with minimal vertical difference in sintering temperature in the sample (Fig. 3 line 1). However, if the die was displaced downwards to form electric and thermal contact between the die and bottom graphite insert, a temperature gradient appeared in the sample (Fig. 3, line 2). Such displacement of the die leads to geometrical asymmetry of the mold and changes the specific electric and thermal resistances of the mold elements, and thereby asymmetrical distributions of the electric and thermal fields; The electric and thermal specific resistivities decrease in the lower part but increase in the upper one.

Greater mold asymmetry leads to higher values of $\Delta T_{z\ sint}$. To achieve this, a die with an extended bottom can be used. Modeling of the sintering process with different die configurations was used to study the influence of the die bottom configuration on the temperature distribution (Fig. 4). A maximum current density value was selected to keep the temperature in the central point of the lower surface of the sample equal to 730 K. The highest $\Delta T_{z\ sint}$ value was achieved for the mold with the step-profile die (Fig. 3, line 6).

Increase of $\Delta T_{z\ sint}$ leads to simultaneous growth of the sintering temperature difference in radial direction $\Delta T_{r\ sint}$. Maximum $\Delta T_{r\ sint}$ values were observed on the upper surface of the samples. The distribution of $\Delta T_{r\ sint}$ along the radius of the upper sample surface for different die configurations is shown in Fig. 5. The geometric parameters of the sample (such as diameter, height, and diameter-to-height ratio) can be varied to decrease the $\Delta T_{r\ sint}$ values. Figure 6 illustrates the drop of radial temperature differences caused by reduction of sample size. The decrease of $\Delta T_{r\ sint}$ is more significant compared with the decrease of $\Delta T_{z\ sint}$.

It is important to trace the change of temperature difference in the sample within the sintering time. We checked how the maximum $\Delta T_{z\ sint}$ changes during the SPS process in a setup with the step-profile die. The temperature in the sample changes proportionally to the current density value with the maximum $\Delta T_{z\ sint}$ remaining almost constant during the holding period. The experimental current mode (Fig. 7a, line 1) seems unsuitable for sintering in a mold with an extended die, because the values of T_{sint} are insufficient for Bi_2Te_3 treatment. The rise in $\Delta T_{z\ sint}$ in this case reaches 80 degrees (Fig. 7 a, line 2) according to the simulation. To achieve a sufficient T_{sint} and increase $\Delta T_{z\ sint}$, the current density was increased by about 1.5 times (Fig. 7b, line 1), which led to a $\Delta T_{z\ sint}$ increase up to 160 degrees (Fig. 7b, line 2).

It seems that the direction of current also has an impact on the ΔT_{sint} values. This influence can be explained by the presence of the Seebeck effect. To confirm this assumption, the calculation was carried out for a sample with h_s = 10 mm and d_s = 20 mm, sintered in the step-profiled die. The maximum values of $\Delta T_{z\ sint}$ and $\Delta T_{r\ sint}$ increased up to 220 K and 70 K.

Note that, during the SPS process in the gradient temperature field, one thermocouple should be located in the graphite die, close to the upper surface of the sample. In this case, the automatic SPS system maintains required current values in order to obtain maximum temperature on the upper surface of the sample. The second thermocouple (if

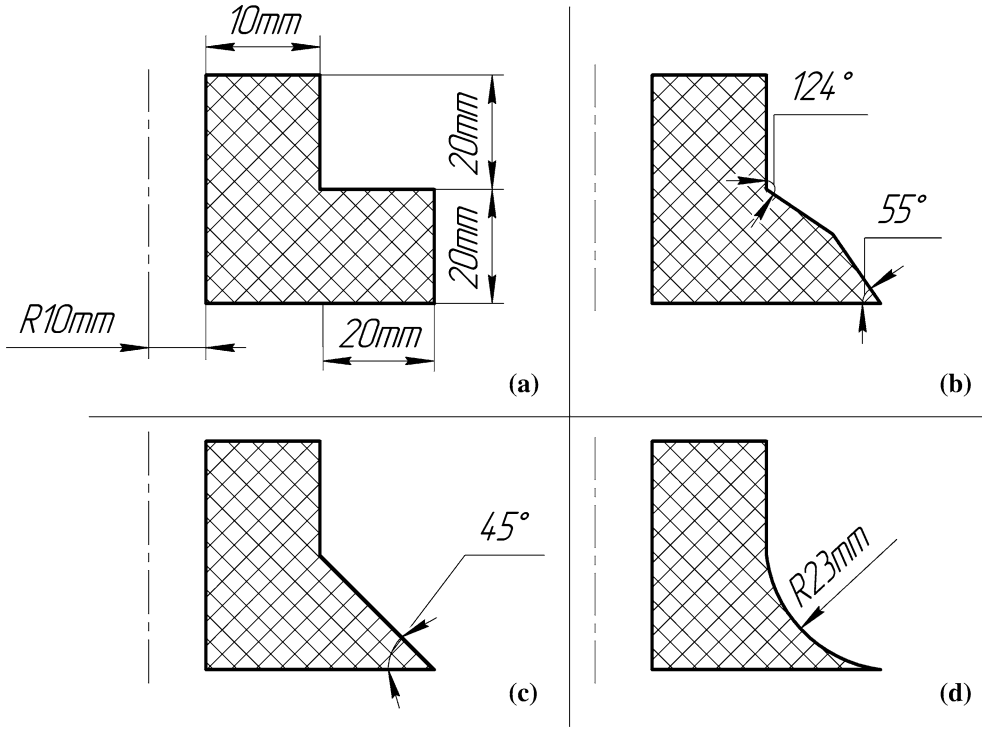

Fig. 4. Different profiles of extension of die bottom part: (a) step, (b) curved, (c) conic, and (d) concave.

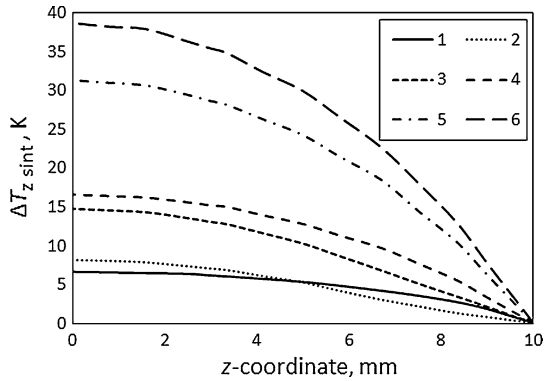

Fig. 5. Temperature distribution at $t = 450$ s along radial axis on upper surface of sample sintered in die with: 1, cylindrical profile (without any extension) and located as shown in Fig. 1; 2, cylindrical profile and in contact with lower graphite insert; 3, concave profile; 4, conic profile; 5, curve profile; 6, step profile.

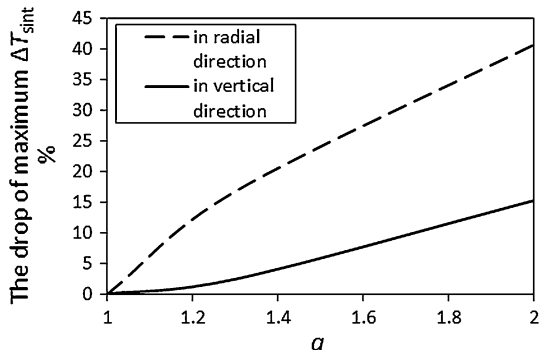

Fig. 6. Drop of temperature differences in radial and vertical direction caused by reduction of sample size in comparison with size of initial sample with $h_{s\ initial} = 10$ mm and $d_{s\ initial} = 20$ mm. The ratio $a = h_s/h_{s\ initial} = d_s/d_{s\ initial}$.

possible) should be placed in the die, close to the lower surface of the sample, in order to trace the temperature value.

CONCLUSIONS

Simulations of the SPS process showed that changing the geometry of the compression mold can enable the current flow in the volume of the setup to be tailored, resulting in a nonuniform temperature field and release of Joule heat within the sample. Therefore, the die of the compression mold not only functions as a mechanical terminator, but also affects the formation of the thermal and electric fields. Vertical temperature differences up to hundreds of degrees can be achieved and maintained during sintering in an asymmetrically located die with extended bottom, being sufficient for one-step SPS processing of thermoelectrics based on Bi_2Te_3/$PbSe_{0.5}Te_{0.5}$, $Bi_{0.3}Sb_{1.7}Te_3/Zn_4Sb_3$, $Bi_2Te_3/CoSb_3$, and other compositions. It seems that the current required for SPS processing of thermoelectrics in an extended die should be increased in comparison with that applied for sintering in a symmetric mold, to obtain significant $\Delta T_{z\ sint}$. This vertical temperature difference increase is accompanied by simultaneous radial temperature difference growth. This could lead to radial inhomogeneity of the sintered material and reduction of the thermoelectric and mechanical

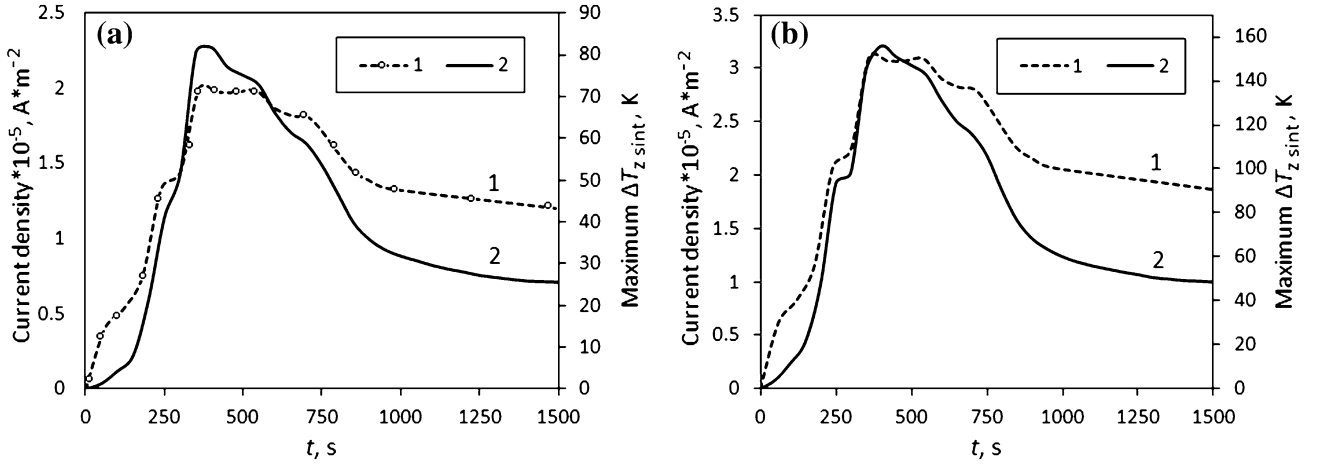

Fig. 7. Time dependence of current density (1) and maximum vertical temperature difference (2) obtained in step-profiled die with experimental (a) and increased (b) current modes; Increased current values and temperature differences were derived from the simulation; h_s = 10 mm d_s = 20 mm.

properties on the periphery of the sample. Addressing this issue remains an additional task related to the $\Delta T_{r\ sint}$ reduction. It is likely that the $\Delta T_{r\ sint}$ increase could be reduced by variation of the geometric parameters of the sample. The results of this work show that it is possible to achieve the thermal conditions required for sintering of inhomogeneous material within a single SPS technological cycle. This approach will also be applicable to other combinations of materials having other requirements in terms of T_{sint} and $\Delta T_{z\ sint}$, although it is likely that different values of current density and sintering duration would be required.

ACKNOWLEDGEMENTS

This work was financially supported by Government of Russian Federation (Grant 074-U01).

REFERENCES

1. O. Guillon, J. Gonzalez-Julian, B. Dargatz, T. Kessel, G. Schierning, J. Räthel, and M. Herrmann, *Adv. Eng. Mater.* 16, 7 (2014).
2. B. Poudel, Q. Hao, Y. Ma, Y. Lan, A. Minnich, B. Yu, X. Yan, D. Wang, A. Muto, D. Vashaee, X. Chen, J. Liu, M.S. Dresselhaus, G. Chen, and Z. Ren, *Science* 320, 634 (2008).
3. L.P. Bulat, I.A. Drabkin, V.V. Karatayev, V.B. Osvenskii, YuN Parkhomenko, D.A. Pshenai-Severin, and A.I. Sorokin, *J. Electron. Mater.* 43, 2121 (2014).
4. L.P. Bulat, V.B. Osvenskii, YuN Parkhomenko, and D.A. Pshenay-Severin, *J. Electron. Mater.* 45, 1648 (2016).
5. L.I. Anatychuk and L.P. Bulat, *Thermoelectrics Handbook: Macro to Nano-Structured Materials*, ed. D.M. Rowe (CRC Press: New York, 2006), p. 930.
6. V.L. Kuznetsov and P.P. Edwards, *ChemSusChem* 3, 44 (2010).
7. T. Caillat, A. Borshchevsky, J. Snyder, and J. Fleurial, *AIP Conf. Proc.* 552, 1107 (2001).
8. S. Yoon, J. Cho, H. Koo, S. Bae, S. Ahn, G.R. Kim, J.S. Kim, and C. Park, *J. Electron. Mater.* 43, 414 (2014).
9. H.S. Kim, K. Kikuchi, T. Itoh, T. Iida, and M. Taya, *Mater. Sci. Eng. B* 185, 45 (2014).
10. K.T. Wojciechowski, R. Zybala, J. Leszczynski, P. Nieroda, M. Schmidt, R. Gajerski, and E. Alexandrova, *AIP Conf. Proc.* 1449, 467 (2012).
11. S. Li, J. Pei, D. Liu, L. Bao, J.F. Li, H. Wu, and L. Li, *Energy* 113, 35 (2016).
12. L.P. Bulat, I.A. Nefedova, and D.A. Pshenay-Severin, *Adv. Sci. Tech.* 93, 168 (2014).
13. L.P. Bulat, A. Drabkin, A.V. Novotelnova, V.B. Osvenskii, Y.N. Parkhomenko, D.A. Pshenai-Severin, A.I. Sorokin, and I.A. Nefedova, *Tech. Phys. Lett.* 40, 11 (2014).
14. L.P. Bulat, A.V. Novotelnova, D.A. Pshenai-Severin, V.B. Osvenskii, A.I. Sorokin, A.V. Asach, and A.S. Tukmakova, *Tech. Phys.* 61, 68 (2016).
15. L.P. Bulat, A.V. Novotelnova, A.V. Asach, A.S. Tukmakova, V.B. Osvenskii, Y.N. Parchomenko, L. Zhao, and Q. Zongrui, *J. Electron. Mater.* 45, 2891 (2016).
16. A.G. Samoilovich and L.L. Korenblit, *Usp. Fiz. Nauk.* 49, 243 (1953).
17. G. Maizza, G.D. Mastrorillo, S. Grasso, H. Ning, and M.J. Reece, *J. Mater. Sci.* 52, 10341 (2017).
18. R.H. Bogaard, P.D. Desai, H.H. Li, and C.Y. Ho, *Thermochim. Acta* 218, 373 (1993).
19. R.S. Graves, T.G. Kollie, D.L. McElroy, and K.E. Gilchrist, *Int. J. Thermophys.* 12, 409 (1991).